CHEMISTRY OF MATERIALS

pubs.acs.org/cm Article

# Ultralow Thermal Conductivity and Thermoelectric Properties of $Rb_2Bi_8Se_{13}$

Songting Cai, Shiqiang Hao, Yubo Luo, Xianli Su, Zhong-Zhen Luo, Xiaobing Hu, Christopher Wolverton, Vinayak P. Dravid,* and Mercouri G. Kanatzidis*

Cite This: https://dx.doi.org/10.1021/acs.chemmater.0c00703 Read Online

ACCESS | Metrics & More | Article Recommendations | Supporting Information

**ABSTRACT:** Complex bismuth chalcogenides are narrow band gap semiconductors with intrinsic low thermal conductivity, which exhibit high potential as highly efficient thermoelectric materials. Here, we assess the basic thermoelectric properties of polycrystalline $Rb_2Bi_8Se_{13}$ in the temperature range 300−823 K as well as performance-optimizing strategies. We find that the as-made bulk samples are single phase with the monoclinic crystal structure ($P2_1/m$) and crystallize in layer morphology. The pristine sample exhibits an exceedingly low lattice thermal conductivity of 0.6−0.46 $W{\cdot}m^{-1}{\cdot}K^{-1}$ at 300−823 K, which derives from strong lattice anharmonicity, large Grüneisen parameters, and low phonon velocities induced by the complex crystal structure with heavy atom Bi and a large unit cell. The Cl doping successfully enhances the carrier concentration in $Rb_2Bi_8Se_{13}$ with a negligible impact on the electronic band structure, displaying common doping behaviors. Se vacancy, on the contrary, leads to n-type doping and enhances the effective mass and power factors more significantly. Consequently, a maximum $ZT$ of ∼0.75 at 823 K for the 0.3% Se-vacancy-doped sample is obtained.

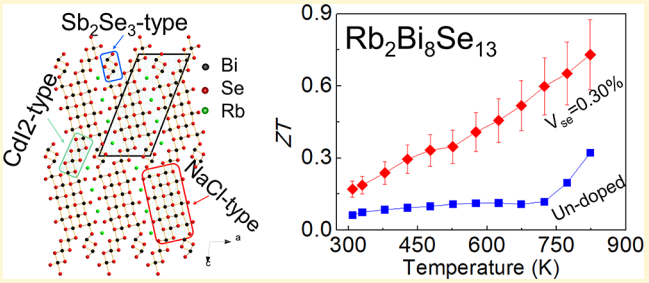


## INTRODUCTION

Thermoelectric materials can enable direct conversion between thermal and electrical energies and can impact waste heat recovery.[1−3] Nevertheless, low efficiency has limited the application range and mass production of TE devices.[1,4] The conversion efficiency is determined by the dimensionless figure of merit, $ZT = S^2\sigma T/\kappa_{tot} = S^2\sigma T/(\kappa_e + \kappa_{latt})$, where $S$ is the Seebeck coefficient, $\sigma$ is the electrical conductivity, $\kappa_{tot}$ is the total thermal conductivity, $T$ is the absolute temperature, and $\kappa_{tot}$ is the sum of electrical ($\kappa_e$) and lattice ($\kappa_{latt}$) thermal conductivities of the materials. Because the parameters in the equation of $ZT$ are interrelated, it makes independent optimization of these three parameters extremely challenging.[1−6]

To optimize the thermoelectric performance, on one hand, enhancement of the power factor (PF = $S^2\sigma$) through band structure engineering (including dopant engineering,[7−12] band convergence,[13−21] band flattening and resonant state induction for effective mass increase,[19,22−29] or texturing for carrier mobility improvement[30]) has been widely applied in a variety of well-known narrow band gap semiconductors such as lead chalcogenides,[31−35] I−V−$VI_2$ compounds (I = Cu, Ag, Au, or alkali metal; V = As, Sb, or Bi; VI = Se or Te),[36,37] $Bi_2Te_3$,[38] lead antimony silver telluride (LAST)[39] and skutterudite.[40] On the other hand, low lattice thermal conductivity could be obtained by either architecture engineering at all length scales[4,34,35,41−45] or in special materials with a high degree of structural complexity.[46−48] SnSe is a good example for the latter, where the large lattice anharmonicity and complex layered crystal structure play significant roles in its ultralow intrinsic thermal conductivity.[6,41,49−53]

In this context, the narrow band gap compounds $A_2Bi_8Se_{13}$ (A = K, Rb, and Cs) possess significant structural and compositional complexity to be considered as potential thermoelectric materials.[47,54,55] Among these, $\beta$-$K_2Bi_8Se_{13}$ has drawn great attention because of its low intrinsic thermal conductivity and high Seebeck coefficient. Studies regarding the synthesis, crystal structure, basic transport properties, and thermoelectric performance enhancement of $\beta$-$K_2Bi_8Se_{13}$ have been reported, with a high peak $ZT$ ∼ 1.3 obtained at 873 K via Cl doping.[54] $Rb_2Bi_8Se_{13}$ crystallizes in a complex low-symmetry monoclinic structure (space group $P2_1/m$), which is different from that of $\beta$-$K_2Bi_8Se_{13}$.[47] To date, only the crystal structure and low-temperature thermoelectric properties have been reported for $Rb_2Bi_8Se_{13}$.

In this work, we synthesized polycrystalline $Rb_2Bi_8Se_{13}$ from high-temperature melting reactions and prepared suitable

Received: February 18, 2020
Revised: March 27, 2020
Published: March 27, 2020

specimens for charge and thermal transport investigations using spark plasma sintering (SPS). We report here for the first time advanced microstructural characterization, doping strategies, and phonon/band structure investigation for this system. The as-made pristine samples of $Rb_2Bi_8Se_{13}$ exhibit n-type semiconducting behavior with extremely low thermal conductivity. The intrinsic $ZT$ value is ~0.26 at 823 K; however, the introduction of Se vacancies or doping with Cl on the Se sites is effective in enhancing the electron carrier concentration and the power factor, leading to a maximum $ZT$ of ~0.75 at 823 K.

## EXPERIMENTAL SECTION

**Synthesis and Processing.** The synthesis procedure of the $Rb_2Bi_8Se_{13}$-based ingot (~12 g) includes two steps. First, $Rb_2Se$ was synthesized through the stoichiometric reaction of Rb (99.99%, Aldrich Chemical) and Se (99.99%, American Elements) under liquid ammonia.[47] Note that an excess of ~2% Se was added to make sure that Rb is fully reacted. Second, $Rb_2Se$, Bi shot (99.999%, American Elements), Se pellets, and $BiCl_3$ powder (99.99%, Alfa Aesar) were mixed according to the nominal composition $(Rb_2Bi_8Se_{13(1-x)})Cl_{13x}$, where $x$/Cl = 0, 0.05, 0.07, 0.15, 0.20%, and $Rb_2Bi_8Se_{13(1-y)}$, where $y/V_{Se}$ = 0,0.05, 0.15, 0.30, 0.45, and 0.70%). The mixed starting materials were flame-sealed in carbon-coated quartz tubes under vacuum (~$2 \times 10^{-3}$ Torr), heated to 1023 K over a period of 15 h, soaked at this temperature for 10 h, and then water-quenched.

The reacted ingots were hand-ground into fine powders and filled into a graphite die (12.7 mm in diameter). The powders were densified using the spark plasma sintering technique (SPS-211LX, Fuji Electronic Industrial Co. Ltd.) under vacuum, at 823 K with a uniaxial compressive pressure (40 MPa) for 6 min. For structural homogenization, the obtained pellets (>91% of the theoretical density) were then annealed at 823 K for 12 h.

**Scanning/Transmission Electron Microscopy(S/TEM) Characterization.** Scanning electron microscopy (SEM) analyses were applied with a tungsten filament SEM (Hitachi S-3400N-II) under 15 kV. Scanning/transmission electron microscopy (S/TEM) and energy dispersive spectroscopy (EDS) analyses were carried out using an aberration-corrected JEOL ARM200F microscope operated at 200 kV. The electron-beam-transmitted TEM specimens were prepared with Ar-ion milling (3 kV for ~30 min, followed by ion cleaning with 0.3 kV for 45 min) under low temperature with a liquid nitrogen stage.

**Electrical Transport Property Measurement.** The electrical conductivities and Seebeck coefficients were measured simultaneously by a ZEM-3 system (Ulvac Riko, Japan) under a low-pressure helium atmosphere (300−823 K). The samples used for measurements were prepared into ~$11 \times 3 \times 3$ $mm^3$ bars and coated with a thin layer of boron nitride (~0.1 mm) for equipment protection. The uncertainties of the Seebeck coefficient and electrical conductivity measurements are ~3 and 5%, respectively.

**Thermal Transport Property Measurement.** The thermal conductivities were calculated based on the equation $\kappa = D \cdot C_p \cdot \rho$, where $D$ is the thermal diffusivity, $C_p$ is the specific heat, and $\rho$ is the density. The thermal diffusivity ($D$) was determined by a laser flash analysis instrument (LFA-457, Netzsch, Germany) under $N_2$ flow. The samples used for $D$ measurements were prepared into pellets with dimensions ~$6 \times 6 \times 1.2$ $mm^3$. The specific heat of the samples was estimated by $C_p = 3R/M$ ($R$: ideal gas constant and $M$: average molar mass of each element). The densities of the samples were calculated by their dimensions and masses. Combining the uncertainty of measurements from $D$ (5%), $\rho$ (5%), and the electrical measurements, the uncertainty for the $ZT$ determination is ~20%.

## RESULTS AND DISCUSSION

**Crystallographic and Microstructural Anisotropy.** $Rb_2Bi_8Se_{13}$ adopts a complex low-symmetry monoclinic crystal structure with the space group $P2_1/m$.[47] As illustrated in Figure 1, $Rb_2Bi_8Se_{13}$ has a three-dimensional framework with rectangular NaCl-type building blocks connected by $Sb_2Se_3$-type and $CdI_2$-type fragments. The connection between different types of building blocks forms small parallel tunnels along the $b$-axis, which are filled with $Rb^+$ ions.[47] Polycrystalline $Rb_2Bi_8Se_{13}$ was prepared by a high-temperature melting reaction. To enhance its electrical transport properties, we synthesized Cl-doped $Rb_2Bi_8Se_{13(1-x)}Cl_{13x}$ samples, where $x$/Cl = 0, 0.05, 0.07, 0.15, and 0.20%, and Se-deficient $Rb_2Bi_8Se_{13(1-y)}$, where $y/V_{Se}$ = 0, 0.05, 0.15, 0.30, 0.45, and 0.70%, using the same procedure as for pure $Rb_2Bi_8Se_{13}$.

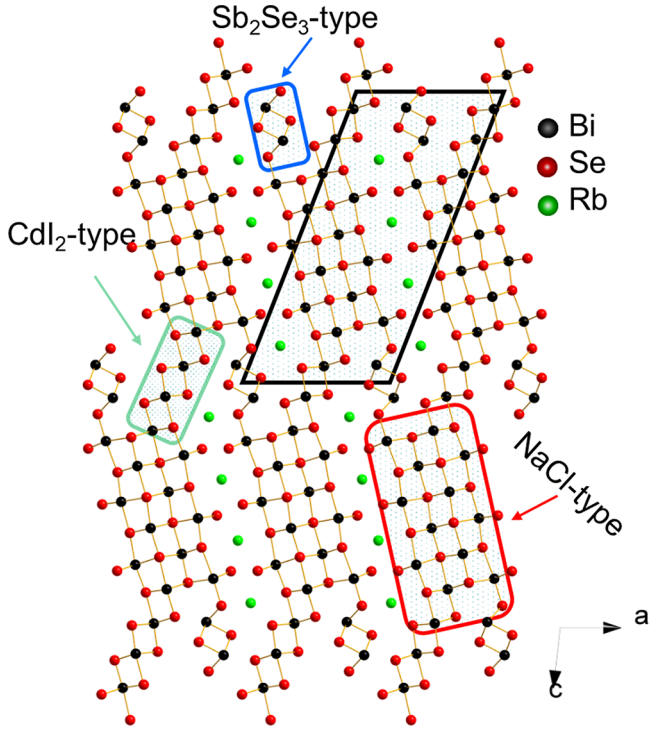


**Figure 1.** Crystal structure of $Rb_2Bi_8Se_{13}$ projected along the $b$-axis ([010] direction) with the unit cell highlighted in black. The three-dimensional (3D) framework consists of infinite NaCl-type blocks (red rectangle) parallel to the $b$-axis, which are connected by $CdI_2$-type (green rectangle) and $Sb_2Se_3$-type fragments (blue rectangle). $Rb^+$ ions fill the tunnels between different building blocks.[47]

Powder X-ray diffraction patterns of all synthesized samples after spark plasma sintering (SPS) are shown in Figure S1a,b. All diffraction peaks can be well-indexed to the $Rb_2Bi_8Se_{13}$ phase as compared to the simulation results (ICSD #92862). A slight shift to a higher diffraction angle is observed with increased doping amount because of lattice contraction after Cl doping or adding Se vacancies.

To study the microstructural anisotropy of the samples after SPS, fresh fractured surfaces of $Rb_2Bi_8Se_{12.9935}$ ($V_{Se}$ = 0.05%) along different orientations with respect to the SPS pressing direction were investigated through scanning electron microscopy (SEM). It is noted that the fractography of all samples is nearly the same; thus, we only show $Rb_2Bi_8Se_{12.9935}$ here as a representative. The fresh fractured sample exhibits grains of $Rb_2Bi_8Se_{13}$ that are arranged in a "layered" fashion; see the inset in Figure 2f. When applying uniaxial pressure (SPS), the grains of $Rb_2Bi_8Se_{13}$ tend to arrange in the plane normal to SPS (in-plane) and form rectangular sheets, Figure 2a−c. The longer dimension of the grain sheets represents the $b$-axis


https://dx.doi.org/10.1021/acs.chemmater.0c00703
Chem. Mater. XXXX, XXX, XXX−XXX

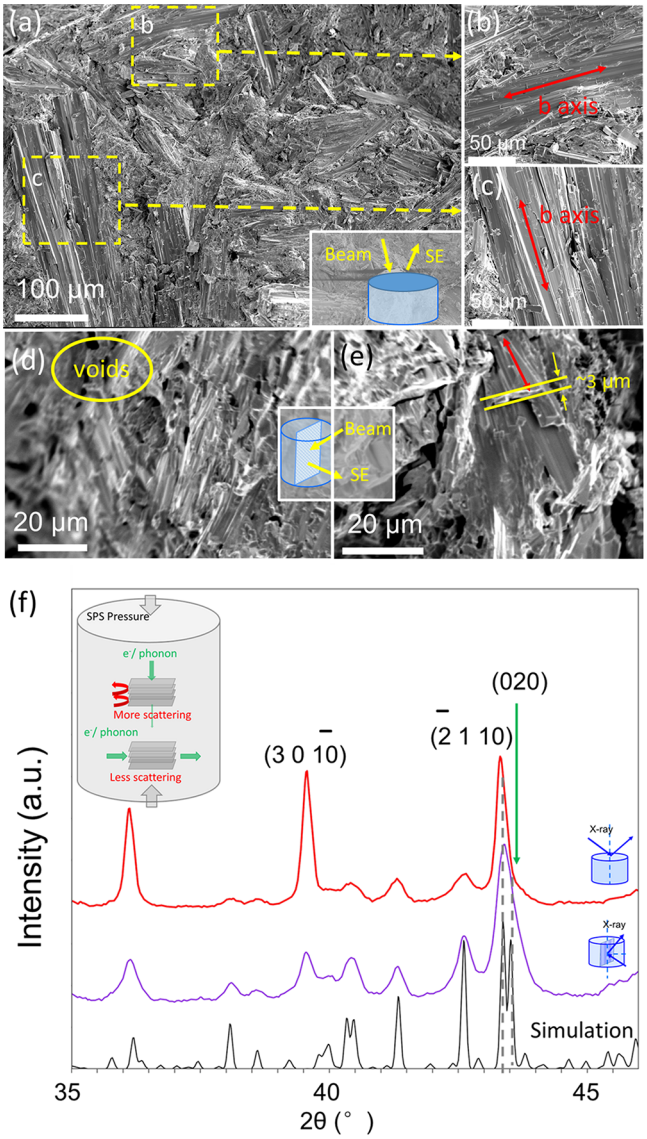


**Figure 2.** Microstructural anisotropy in $Rb_2Bi_8Se_{13}$-based samples. (a) SEM (SE) image of the fresh fractured surface of $Rb_2Bi_8Se_{12.9935}$ ($V_{Se}$ = 0.05%) normal to the SPS direction (in-plane). Grains like rectangular sheets can be observed, and the sheets tend to stack along the SPS pressing direction. (b, c) Two zoom-in views of (a) with two different grain orientations, where *b*-axes are labeled with red arrows (the longest grain orientation). (d, e) SEM images of the surface parallel to the SPS direction (out-plane). A higher degree of porosity between different stacks of sheets is observable. The width of each sheet is ~1 $\mu$m. (f) X-ray diffraction patterns of the in-plane (red) and out-plane (purple) surfaces of the $Rb_2Bi_8Se_{13}$ sample, which indicate its anisotropic feature. The schematic inset at the upper left corner illustrates the grain arrangements.

direction, which can grow into hundreds of microns in length, whereas the other dimension in this plane is ~20 $\mu$m. It is noteworthy that the *b*-axes are randomly distributed in-plane without any preference. Moreover, the sheet-like crystallites organize to form a "layer" morphology along the SPS direction, see Figure 2c, where part of the sheet on the top layer is broken and the underneath one is visible. According to the SEM image of the surface parallel to the SPS direction (out-plane), the width of each layer is ~1 $\mu$m. In addition, a higher degree of porosity can be observed between different stackings of sheets. X-ray diffraction along these two directions confirms this anisotropy, Figure 2f. More details on the degree of orientation can be found in the Supporting Information. Electronic and heat carriers experience more scattering when passing through more boundaries, leading to lower thermal/electrical conductivity along the SPS pressing direction, Figure S4.

A detailed investigation of the microstructure in the $Rb_2Bi_8Se_{13}$-based system was performed using scanning/transmission electron microscopy (S/TEM) analyses. Figure 3a is a typical low-magnification annular dark field (ADF) STEM image of the $Rb_2Bi_8Se_{12.961}$ ($V_{Se}$ = 0.30%) sample, showing both mass contrast (Z-contrast) and diffraction contrast of the specimen. The inset selected area electron diffraction (SAED) pattern belongs to monoclinic $Rb_2Bi_8Se_{13}$ (space group: $P2_1/m$) along the [100] zone axis. No diffraction spot splitting, extra/super spots, or streaking is observed, confirming the single-phase nature of the material. Moreover, a layered microstructure with ~1−3 $\mu$m in width agrees with the height of each sheet shown in the SEM results above. The chemical analysis with energy-dispersive spectroscopy (EDS) mappings indicates that all elements distribute uniformly across the sample, with an average composition of $Rb_2Bi_{7.9}Se_{12.86}$, close to the nominal one.

In addition, aberration-corrected high-resolution STEM (HRSTEM) was performed to understand the atomic arrangement in the complex crystal structure. Figure 3b is the high-angle annular dark field (HAADF) image taken along the [100] zone axis, where a layered atomic structure is observable. The inset shows a zoom-in version of Figure 3b with atom species labeled for clarification. Specifically, the structure along the [100] zone axis can be divided into two types of alternating layers: In layer type I, the adjacent Bi atom planes in projection appear very close (~1 Å), whereas relatively farther apart in layer type II (~3 Å). Se and Rb atomic columns are also detectable with lower brightness. HRSTEM images (bright field) along another high-index axis taken from the Cl-doped sample show further confirmation of the crystal structure (Figure S2a,b).

**Electrical Properties of Undoped and Electron-Doped $Rb_2Bi_8Se_{13}$.** Because of the anisotropic microstructure discussed above, the thermoelectric properties of $Rb_2Bi_8Se_{13}$ are orientation-dependent. Therefore, in this study, all transport properties were measured along the direction perpendicular to the applied pressure of SPS. The temperature-dependent electrical properties of undoped $Rb_2Bi_8Se_{13}$ are shown with black lines in Figure 4a−f. According to the electrical conductivity results, the undoped $Rb_2Bi_8Se_{13}$ behaves as a slightly doped semiconductor. By "undoped", we refer to the sample obtained as prepared without any deliberate effort to dope it. Typically, the electrical conductivity ($\sigma$) at room temperature is very low ~20 S cm$^{-1}$ and gradually decreases to 15 S·cm$^{-1}$ at 623 K, after which bipolar diffusion is obvious and $\sigma$ starts to increase and reaches ~25 S·cm$^{-1}$ at 823 K. The Seebeck coefficient across the whole testing temperature range is consistently negative, indicating its n-type semiconducting nature. Moreover, the absolute value of the Seebeck coefficient changes with temperature as the opposite of conductivity, as expected, with a maximum value ~−320 $\mu$V·K$^{-1}$ obtained at 523 K. However, due to the poor conductivity, the power factor of the undoped sample is less than 2 $\mu$W·cm·K$^{-1}$ at 823 K. Therefore, we utilized known n-type dopants for other bismuth chalcogenides, namely, Cl and Se-vacancy doping,[46,54] to improve the electrical properties of $Rb_2Bi_8Se_{13}$.


https://dx.doi.org/10.1021/acs.chemmater.0c00703
Chem. Mater. XXXX, XXX, XXX−XXX

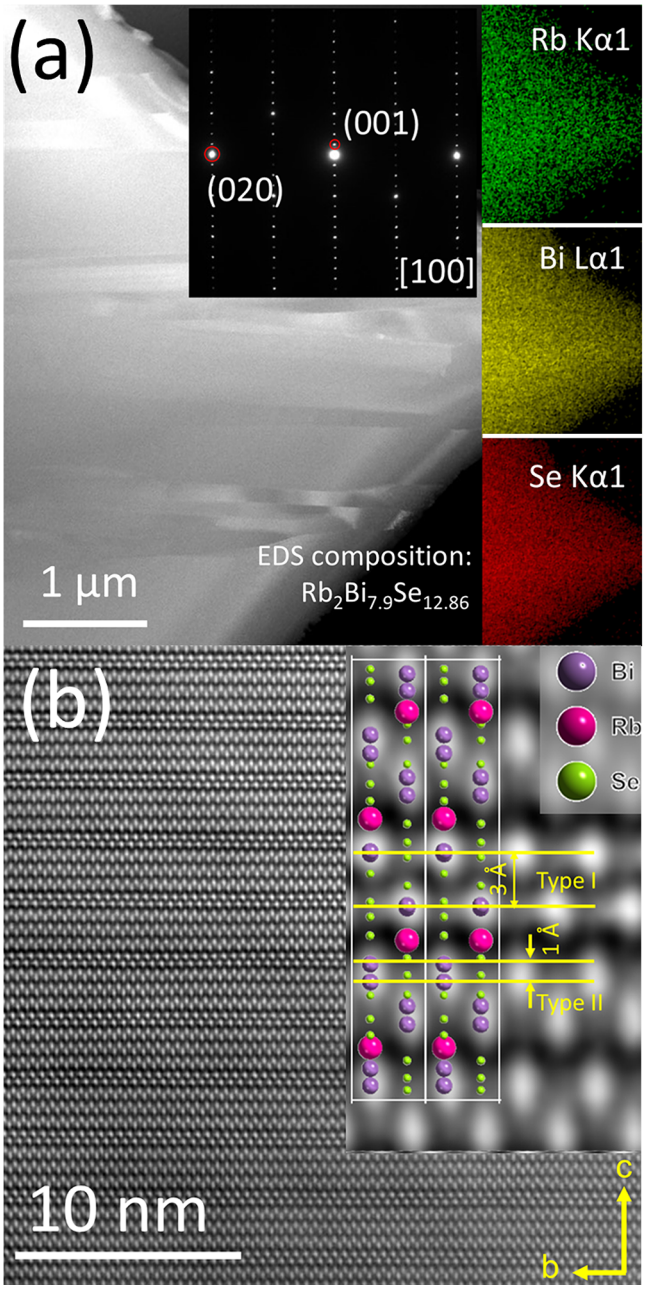


**Figure 3.** S/TEM analyses of $Rb_2Bi_8Se_{13}$-based materials. (a) Low-magnification annular dark field (ADF) image of the $Rb_2Bi_8Se_{12.961}$ ($V_{Se}$ = 0.30%) sample, with the corresponding selected area electron diffraction (SAED) pattern and EDS mappings shown in the inset. (b) Atomic-resolution high-angle annular dark field (HAADF) image taken along the [100] zone axis. The inset is a zoom-in view with the atom position labeled. Two types of alternating atomic layers with significantly different Bi plane distances are highlighted.

Upon Cl doping, the electrical conductivity is significantly enhanced with increasing Cl concentration, Figure 4a. Specifically, the room temperature $\sigma$ of the 0.2% Cl (Cl = 0.20%) sample increased from 18 to ~340 S·cm$^{-1}$, which indicates that Cl has been successfully doped into the $Rb_2Bi_8Se_{13}$ lattice. Generally, the $\sigma$ of all Cl-doped samples first gradually decreases with temperature until 523 K and then slightly increases because of bipolar diffusion. Moreover, owing to the increase of carrier concentration, the absolute values of Seebeck coefficients are lower than that of the undoped

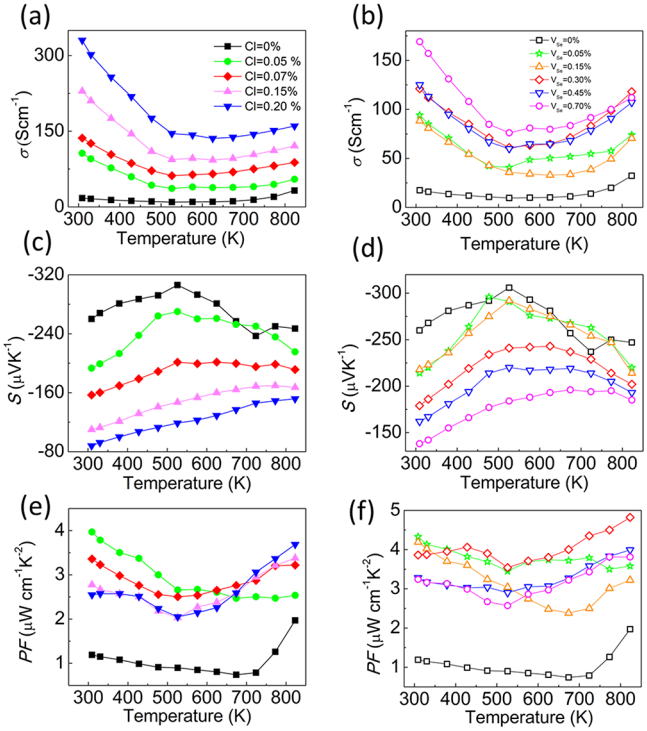


**Figure 4.** Temperature-dependent (a, b) electrical conductivity, (c, d) Seebeck coefficient, and (e, f) power factor of Cl-doped ($Rb_2Bi_8Se_{13(1-x)}Cl_{13x}$, where $x$/Cl = 0, 0.05, 0.07, 0.15, and 0.20%) and Se-deficient ($Rb_2Bi_8Se_{13(1-y)}$, where $y/V_{Se}$ = 0, 0.05, 0.15, 0.30, 0.45, and 0.70%) samples, respectively. The uncertainties of the Seebeck coefficient and electrical conductivity measurements are ~3 and 5%, respectively.

sample, Figure 4c. For instance, the Seebeck coefficient of the Cl = 0.07% sample at room temperature is around −150 $\mu$V·K$^{-1}$, which increases to −200 $\mu$V·K$^{-1}$ at 523 K and then decreases slightly to −180 $\mu$V·K$^{-1}$ at 823 K. As a result, the power factors for all samples are enhanced, as shown in Figure 4e. The highest power factor at room temperature obtained in Cl-doped samples is ~4.0 $\mu$W·cm·K$^{-1}$ for Cl = 0.05%, and this value remains essentially unchanged across the testing temperature regime.

Similar to Cl doping, the introduction of Se vacancies in Se-deficient samples also introduces free electrons in the compound, leading to an enhancement of electrical conductivity as the Se-vacancy concentration increases, Figure 4b. However, at comparable carrier concentration (Table S2), the Se-deficient samples exhibit a much higher Seebeck coefficient than the Cl-doped samples. For example, the room-temperature Hall carrier concentration for the $V_{Se}$ = 0.05% sample is ~3.31 × 10$^{19}$ cm$^{-3}$ and its Seebeck coefficient is ~−214 $\mu$V·K$^{-1}$. However, for the Cl = 0.15% sample with similar $n_H$ = ~2.81 × 10$^{19}$cm$^{-3}$, the corresponding Seebeck coefficient of ~−110 $\mu$V·K$^{-1}$ is much lower in the absolute value.

We further calculated the room-temperature effective masses ($m^*$) for the samples based on the Pisarenko relation[5] and assumed a single parabolic band contributing to carrier conduction. The results indicate that significantly higher effective masses are obtained through Se vacancy when comparing to Cl doping. Specifically, the room-temperature effective mass increases from ~0.36$m_e$ for the undoped sample to ~1.46$m_e$ for the 0.15% $V_{Se}$ sample, more than 2× of that in the 0.15% Cl sample (0.507$m_e$). As a result, the power factors


https://dx.doi.org/10.1021/acs.chemmater.0c00703
Chem. Mater. XXXX, XXX, XXX−XXX

of Se-deficient samples increased more significantly, with the highest value obtained in the $V_{Se}$ = 0.30% sample of ~5 $\mu$W·cm·K$^{-1}$ at 823 K, Figure 4f.

To understand the differences between Cl doping and Se vacancies and their effects on the transport behaviors of $Rb_2Bi_8Se_{13}$, we performed first principle calculations to study the electronic band structures of $Rb_4Bi_{16}Se_{26}$, $Rb_4Bi_{16}Se_{25}Cl$, and $Rb_4Bi_{16}Se_{25}$, Figure 5a–f. The calculation results indicate

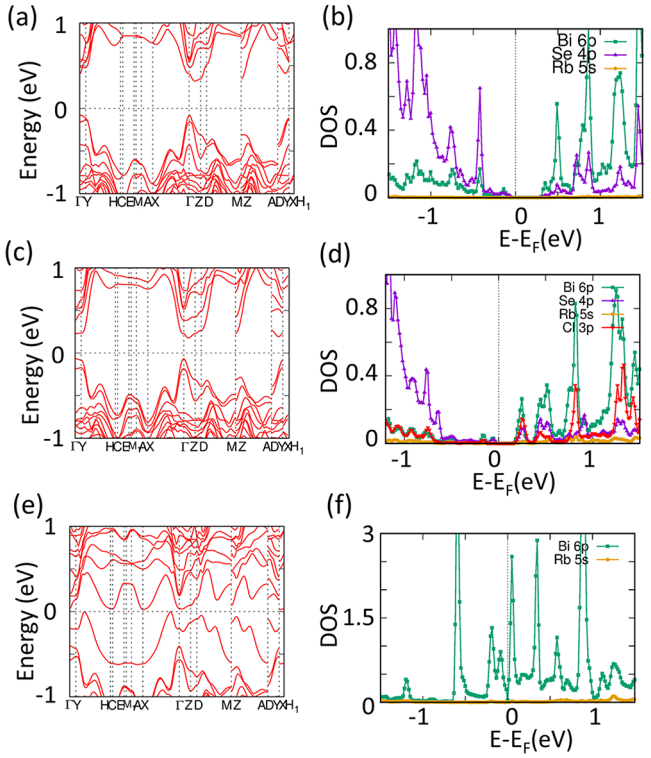


**Figure 5.** (a), (c), (e) Density functional theory (DFT)-calculated electronic band structures and (b), (d), (f) corresponding projected electronic density of states of $Rb_4Bi_{16}Se_{26}$, $Rb_4Bi_{16}Se_{25}Cl$, and $Rb_4Bi_{16}Se_{25}$, respectively.

that pure $Rb_2Bi_8Se_{13}$ is an indirect band gap semiconductor with a band gap of ~0.5 eV, in good agreement with the experimentally measured value of ~0.45 eV (Figure S3). The calculations also reveal a multiband nature for both the valence and conduction bands. The valence band has two closely lying maxima separated by about 0.04 eV in energy, Figure 5a. The first valence band maximum is located at Γ point while the second valence band at Y. There are also two conduction bands at the Z point and a point along Γ–$Z$ with an energy difference of 0.03 eV. The projected density of states depicts the atomic contribution to the band structure, especially for the top portion of the valence band and the bottom portion of the conduction band. For pure $Rb_4Bi_{16}Se_{26}$, the valence band maximum is contributed mainly from Se 4p states and the conduction band minimum is from Bi 6p states, Figure 5b. The contribution of Rb states in the bands near the Fermi level is negligible, suggesting that electron transport in this material is through Bi-based 6p orbitals and hole transport is through Se 4p states.

When substituting some Se with Cl, the band shape of $Rb_4Bi_{16}Se_{25}Cl$ is very close to that of the parent $Rb_4Bi_{16}Se_{26}$, but with a smaller band gap of 0.22 eV, Figure 5c. The corresponding projected density of states (Figure 5d) further indicates that the conduction band minimum of $Rb_4Bi_{16}Se_{25}Cl$ is a hybrid of Bi 6p, Se 4p, and Cl 3p, where the Cl 3p peak is at almost the same position as that of the Se 4p state. Correspondingly, the density of state effective mass of $Rb_4Bi_{16}Se_{25}Cl$ is 0.55$m_e$, very similar to that of the pure sample of 0.53$m_e$. However, for the Se-deficient sample (Figure 5e–f), the band structure changes significantly due to the presence of unbonded Bi 6p electrons. Specifically, relative to pure $Rb_4Bi_{16}Se_{26}$, Se vacancy induces very flat bands around the Fermi level because of the neighbor Bi *6p* electrons, which results in an effective mass of 1.31$m_e$, much larger than that of the undoped and Cl-doped samples mentioned above. The projected DOS of the Se orbital states are not plotted due to very small values.

**Ultralow Thermal Conductivity.** Figure 6 displays the temperature-dependent total and lattice thermal conductivities

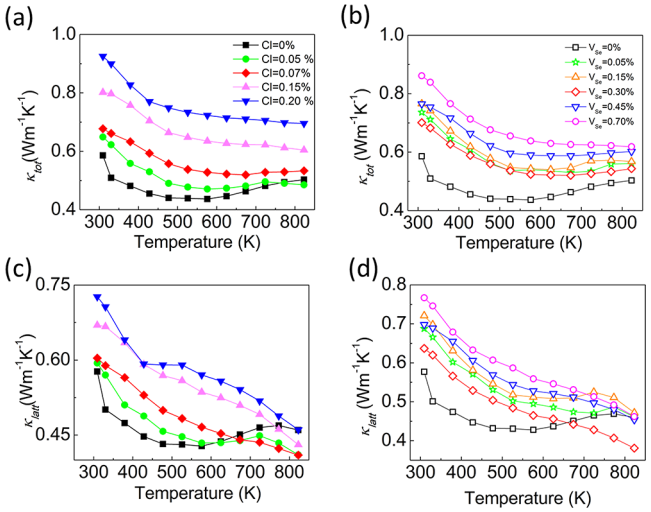


**Figure 6.** Temperature-dependent (a, c) total thermal conductivity and (b, d) lattice thermal conductivity of Cl-doped ($Rb_2Bi_8Se_{13(1-x)}Cl_{13x}$, where $x$/Cl = 0, 0.05, 0.07, 0.15, and 0.20%) and Se-deficient ($Rb_2Bi_8Se_{13(1-y)}$, where $y/V_{Se}$ = 0, 0.05, 0.15, 0.30, 0.45, and 0.70%) samples, respectively. The estimated uncertainty of the thermal transport measurements is ~10%.

of intrinsic, Cl-doped, and Se-vacancy-doped samples. For intrinsic $Rb_2Bi_8Se_{13}$, the total thermal conductivity at room temperature is ~0.6 W·m$^{-1}$·K$^{-1}$ and decreases to lower than 0.45 W·m$^{-1}$·K$^{-1}$ at 573 K, followed by a slight increase from 573 to 823 K due to bipolar diffusion. The lattice thermal conductivity value is very close to $\kappa_{tot}$ because of the negligible electronic contribution ($\kappa_{ele}$). For Cl-doped samples, $\kappa_{tot}$ is slightly increased but maintains low values. Specifically, the room temperature $\kappa_{tot}$ for the Cl = 0.05% sample is around 0.65 W·m$^{-1}$·K$^{-1}$ and falls to ~0.45 W·m$^{-1}$·K$^{-1}$ at 523 K. The sample with 0.05% Cl concentration has the lowest $\kappa_{latt}$, which is only ~0.43 W·m$^{-.1}$K$^{-1}$ at 823 K, Figure 6c. Similar results were obtained for the Se-deficient samples where the introduced vacancy defects preserve the originally low thermal conductivity. For example, the $V_{Se}$ = 0.30% sample has $\kappa_{latt}$ of 0.64 W·m$^{-1}$·K$^{-1}$, which decreases with temperature to 0.37 W·m$^{-1}$·K$^{-1}$ at 823 K, Figure 6b,d.

To understand the mechanism of the low thermal conductivity in $Rb_2Bi_8Se_{13}$, we studied the thermal transport behavior via DFT-based phonon calculations. In short, the calculations reveal that $Rb_2Bi_8Se_{13}$ possesses several advanta-


https://dx.doi.org/10.1021/acs.chemmater.0c00703
Chem. Mater. XXXX, XXX, XXX–XXX

geous features, namely, slow phonon velocities and large Grüneisen parameters, which are beneficial for obtaining low lattice thermal conductivity. From the phonon dispersion relationship shown in Figure 7a, the vibration frequency for the

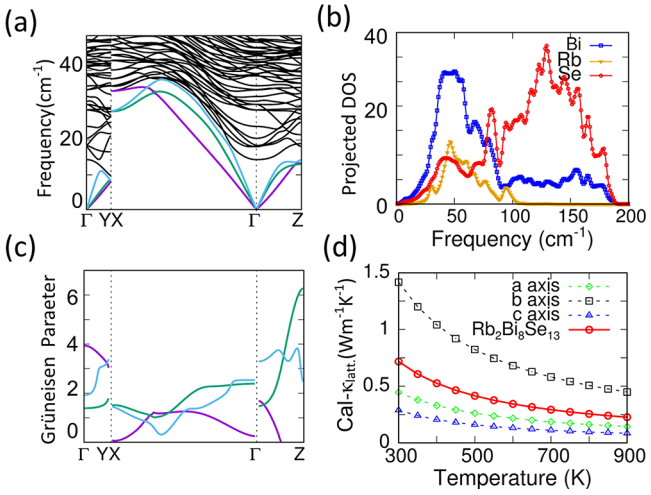


**Figure 7.** (a) Phonon dispersion curves (the colored curves represent acoustic branches) and (b) corresponding projected phonon density of states of $Rb_2Bi_8Se_{13}$. (c) Grüneisen parameters along different reciprocal directions. (d) Calculated lattice thermal conductivity along three crystal directions and average lattice thermal conductivity from 300 to 900 K.

acoustic branches is relatively low. Owing to the larger lattice parameters along *a* (13.49 Å) and *c* (24.71 Å) compared with the *b*-axis (4.16 Å), the vibration energy along Γ−*Z* and Γ−*Y* is even significantly lower than that along the Γ−*X* direction. Moreover, the calculated phonon velocities for TA, TA′, and LA modes (based on the phonon dispersions) along different crystal directions are very low, see Table 1.

**Table 1. Calculated Phonon Velocities $v_{TA}$, $v_{TA'}$, and $v_{LA}$ (m·s$^{-1}$) along the *a*, *b*, and *c* Crystal Directions of $Rb_2Bi_8Se_{13}$, Respectively**

| direction | $v_{TA}$ | $v_{TA'}$ | $v_{LA}$ | average |
|---|---|---|---|---|
| *a* | 1028 | 1946 | 2312 | 1482 |
| *b* | 1358 | 1995 | 2657 | 1958 |
| c | 1442 | 1442 | 3445 | 1560 |

According to the calculated projected phonon density of states (Figure 7b), the acoustic phonon transport (frequency lower than 40 cm$^{-1}$) in $Rb_2Bi_8Se_{13}$ mainly originates from Bi atoms with negligible contribution from Se and Rb. In addition, the Grüneisen parameters of $Rb_2Bi_8Se_{13}$ are large, especially along the *a* and *c* directions (Figure 7c). Specifically, the averaged Grüneisen parameters for TA, TA′, and LA modes are 2.24, 2.38, and 2.54, respectively. Such large values directly reflect strong lattice anharmonicity and anisotropy in the materials. These phonon behaviors mentioned above play positive roles in decreasing lattice thermal conductivity,[56,57] as shown in Figure 7d. The calculated lattice thermal conductivities for $Rb_2Bi_8Se_{13}$ along the *a* and *c* axes are both below 0.46 W·m$^{-1}$·K$^{-1}$ at 300 K, while around 1.4 W·m$^{-1}$·K$^{-1}$ at 300 K along the *b* axis. The average lattice thermal conductivity is ∼0.74 W·m$^{-1}$·K$^{-1}$ at room temperature and decreases to an ultralow value of 0.25 W·m$^{-1}$·K$^{-1}$ at 900 K, in good agreement with the experimental data.

The thermal transport properties of $Rb_2Bi_8Se_{13}$ exhibit a similar trend to $\beta$-$K_2Bi_8Se_{13}$-based materials. The potassium compound exhibits extremely low lattice thermal conductivities of 0.42−0.20 W·m$^{-1}$·K$^{-1}$ between 300 and 873 K.[54] The reasons for this are similar to those of the $Rb_2Bi_8Se_{13}$ compound, but the slightly lower thermal properties of $\beta$-$K_2Bi_8Se_{13}$ may originate from the K/Bi mixed occupancy in its crystal structure or the coexistent minor phase $K_{2.5}B_{8.5}Se_{14}$, contributing further phonon scattering.[54]

**Improved *ZT* via Cl- or Se-Vacancy Doping.** The thermoelectric performance with a peak *ZT* of ∼0.26 at 823 K of undoped $Rb_2Bi_8Se_{13}$ is relatively poor mainly because of low intrinsic electrical conductivity. Because of the enhanced electrical properties and the preserved low thermal conductivity upon Cl-doping and Se-vacancy introduction, a large enhancement in the thermoelectric properties is achieved, Figure 8. For example, when the Cl concentration is 0.07%, the highest *ZT* is around 0.48 at 823 K. For Se-deficient samples, the highest *ZT* of ∼0.75 at 823 K is obtained with $V_{Se}$ = 0.30%

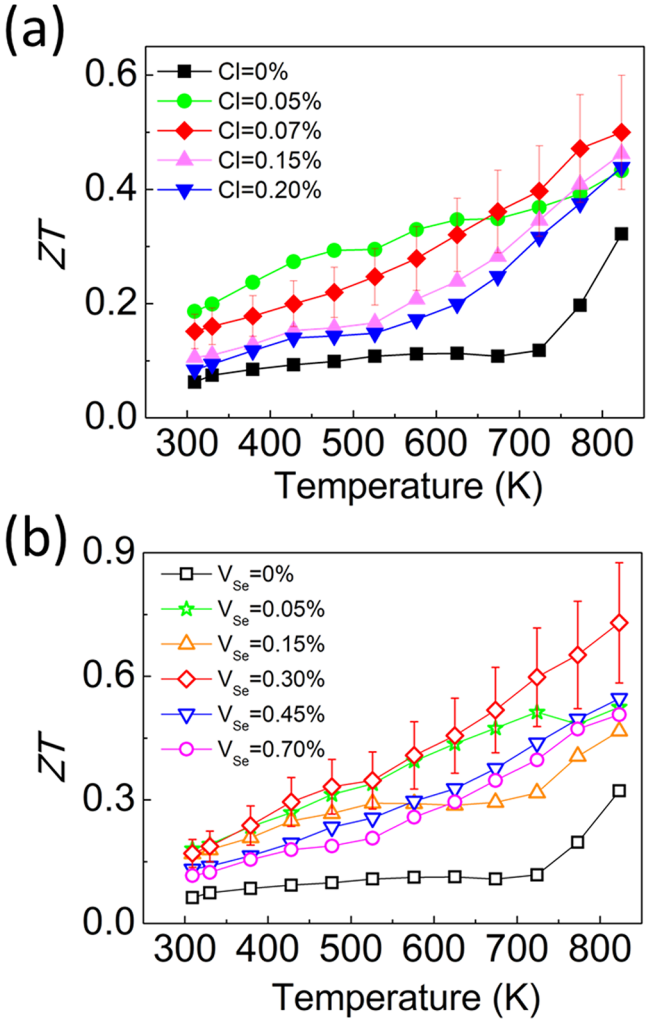


**Figure 8.** Temperature-dependent *ZT* values of (a) Cl-doped ($Rb_2Bi_8Se_{13(1-x)}Cl_{13x}$, where *x*/Cl = 0, 0.05, 0.07, 0.15, and 0.20%) and (b) Se-deficient ($Rb_2Bi_8Se_{13(1-y)}$, where $y/V_{Se}$ = 0, 0.05, 0.15, 0.30, 0.45, and 0.70%) samples.


https://dx.doi.org/10.1021/acs.chemmater.0c00703
Chem. Mater. XXXX, XXX, XXX−XXX

with ∼20% of uncertainty, nearly ∼200% enhancement over the undoped sample.

## CONCLUDING REMARKS

The as-made n-type polycrystalline $Rb_2Bi_8Se_{13}$-based samples crystallize as a single phase with ∼1−100 μm grain size and exhibit high microstructural anisotropy. Both Cl- and Se-vacancy doping can successfully induce n-type carriers into the lattice but affect the electronic band structure differently. According to DFT calculations, the introduction of Se vacancy in $Rb_2Bi_8Se_{13}$ induces very flat bands around the Fermi level due to the existence of unbonded Bi 6p electrons, which enhances the effective mass from $\sim 0.36m_e$ for the undoped sample to $\sim 1.46m_e$ for the 0.15% $V_{Se}$ sample. The undoped $Rb_2Bi_8Se_{13}$ exhibits low lattice thermal conductivity of ∼0.60 $W{\cdot}m^{-1}{\cdot}K^{-1}$ at room temperature, which drops to an ultralow value of ∼0.40 $W{\cdot}m^{-1}{\cdot}K^{-1}$ at 573 K. DFT phonon calculations revealed that such low thermal transport behavior is attributed to strong lattice anharmonicity, slow phonon velocities, and large Grüneisen parameters. On combining the enhanced electrical properties and the low thermal conductivity, a peak *ZT* of ∼0.75 at 823 K for the 0.3% Se-vacancy-doped sample is obtained.

## ASSOCIATED CONTENT

### Supporting Information

The Supporting Information is available free of charge at https://pubs.acs.org/doi/10.1021/acs.chemmater.0c00703.

XRD characterizations; band gap measurements; DFT calculation methods (electronic band structure and phonon dispersion); measured densities; room-temperature Hall carrier density, effective mass, and Hall mobility; STEM images; room-temperature electronic absorption spectrum; thermoelectric properties of the intrinsic sample; diffusivity; Lorenz numbers; and electrical thermal conductivity (PDF)

## AUTHOR INFORMATION


### Corresponding Authors

**Vinayak P. Dravid** − *Department of Materials Science and Engineering and NUANCE Center, Northwestern University, Evanston, Illinois 60208, United States;* orcid.org/0000-0002-6007-3063; Email: v-dravid@northwestern.edu

**Mercouri G. Kanatzidis** − *Department of Chemistry, Northwestern University, Evanston, Illinois 60208, United States;* orcid.org/0000-0003-2037-4168; Email: m-kanatzidis@northwestern.edu

### Authors

**Songting Cai** − *Department of Materials Science and Engineering and Department of Chemistry, Northwestern University, Evanston, Illinois 60208, United States;* orcid.org/0000-0003-2203-5362

**Shiqiang Hao** − *Department of Materials Science and Engineering, Northwestern University, Evanston, Illinois 60208, United States;* orcid.org/0000-0002-7985-4468

**Yubo Luo** − *Department of Chemistry, Northwestern University, Evanston, Illinois 60208, United States; School of Materials Science and Engineering, Nanyang Technological University, 639798, Singapore*

**Xianli Su** − *Department of Chemistry, Northwestern University, Evanston, Illinois 60208, United States;* orcid.org/0000-0003-4428-6461

**Zhong-Zhen Luo** − *Department of Chemistry, Northwestern University, Evanston, Illinois 60208, United States; School of Materials Science and Engineering, Nanyang Technological University, 639798, Singapore;* orcid.org/0000-0003-4331-6286

**Xiaobing Hu** − *Department of Materials Science and Engineering and NUANCE Center, Northwestern University, Evanston, Illinois 60208, United States;* orcid.org/0000-0002-9233-8118

**Christopher Wolverton** − *Department of Materials Science and Engineering, Northwestern University, Evanston, Illinois 60208, United States;* orcid.org/0000-0003-2248-474X

Complete contact information is available at: https://pubs.acs.org/10.1021/acs.chemmater.0c00703


### Notes

The authors declare no competing financial interest.

## ACKNOWLEDGMENTS

This work was primarily supported by the Department of Energy, Office of Science, Basic Energy Sciences under grant DE-SC0014520. This work also made use of the EPIC facility of Northwestern University's NUANCE Center, which has received support from the Soft and Hybrid Nanotechnology Experimental (SHyNE) Resource (NSF ECCS-1542205); the MRSEC program (NSF DMR-1720139) at the Materials Research Center; the International Institute for Nanotechnology (IIN); the Keck Foundation; the State of Illinois through the IIN; and the Office of Science, U.S. Department of Energy under Contract Nos. DE-AC02-06CH11357 and DE-AC02-05CH11231. Access to facilities of high-performance computational resources at the Northwestern University is acknowledged.

## REFERENCES


(1) Snyder, G. J.; Toberer, E. S. Complex thermoelectric materials. *Nat. Mater.* **2008**, *7*, 105−114.

(2) Tan, G.; Zhao, L.-D.; Kanatzidis, M. G. Rationally Designing High-Performance Bulk Thermoelectric Materials. *Chem. Rev.* **2016**, *116*, 12123−12149.

(3) Zeier, W. G.; et al. Thinking Like a Chemist: Intuition in Thermoelectric Materials. *Angew. Chem., Int. Ed.* **2016**, *55*, 6826−6841.

(4) He, J.; Kanatzidis, M. G.; Dravid, V. P. High performance bulk thermoelectrics via a panoscopic approach. *Mater. Today* **2013**, *16*, 166−176.

(5) Zhang, X.; Zhao, L.-D. Thermoelectric materials: Energy conversion between heat and electricity. *J. Materiomics* **2015**, *1*, 92−105.

(6) Chen, Z.-G.; Shi, X.; Zhao, L.-D.; Zou, J. High-performance SnSe thermoelectric materials: Progress and future challenge. *Prog. Mater. Sci.* **2018**, *97*, 283−346.

(7) Kuznetsov, V. L.; Kuznetsova, L. A.; Kaliazin, A. E.; Rowe, D. M. High performance functionally graded and segmented Bi2Te3-based materials for thermoelectric power generation. *J. Mater. Sci.* **2002**, *37*, 2893−2897.

(8) Pei, Y.; Lensch-Falk, J.; Toberer, E. S.; Medlin, D. L.; Snyder, G. J. High Thermoelectric Performance in PbTe Due to Large Nanoscale Ag2Te Precipitates and La Doping. *Adv. Funct. Mater.* **2011**, *21*, 241−249.

(9) Yamini, S. A.; et al. Rational design of p-type thermoelectric PbTe: temperature dependent sodium solubility. *J. Mater. Chem. A* **2013**, *1*, 8725−8730.
(10) Pei, Y.; May, A. F.; Snyder, G. J. Self-Tuning the Carrier Concentration of PbTe/Ag2Te Composites with Excess Ag for High Thermoelectric Performance. *Adv. Energy Mater.* **2011**, *1*, 291−296.
(11) Pei, Y.; et al. Stabilizing the Optimal Carrier Concentration for High Thermoelectric Efficiency. *Adv. Mater.* **2011**, *23*, 5674−5678.
(12) Dashevsky, Z.; Shusterman, S.; Dariel, M. P.; Drabkin, I. Thermoelectric efficiency in graded indium-doped PbTe crystals. *J. Appl. Phys.* **2002**, *92*, 1425−1430.
(13) Tan, G.; et al. Extraordinary role of Hg in enhancing the thermoelectric performance of p-type SnTe. *Energy Environ. Sci.* **2015**, *8*, 267−277.
(14) Zhang, Q.; et al. High thermoelectric performance by resonant dopant indium in nanostructured SnTe. *Proc. Natl. Acad. Sci. U.S.A.* **2013**, *110*, 13261−13266.
(15) Tan, G.; et al. High Thermoelectric Performance of p-Type SnTe via a Synergistic Band Engineering and Nanostructuring Approach. *J. Am. Chem. Soc.* **2014**, *136*, 7006−7017.
(16) Zhang, J.; et al. High-Performance Pseudocubic Thermoelectric Materials from Non-cubic Chalcopyrite Compounds. *Adv. Mater.* **2014**, *26*, 3848−3853.
(17) Banik, A.; Shenoy, U. S.; Anand, S.; Waghmare, U. V.; Biswas, K. Mg Alloying in SnTe Facilitates Valence Band Convergence and Optimizes Thermoelectric Properties. *Chem. Mater.* **2015**, *27*, 581−587.
(18) Pei, Y.; Wang, H.; Snyder, G. J. Thermoelectric Materials: Band Engineering of Thermoelectric Materials (Adv. Mater. 46/2012). *Adv. Mater.* **2012**, *24*, 6124.
(19) Tan, G.; et al. Valence Band Modification and High Thermoelectric Performance in SnTe Heavily Alloyed with MnTe. *J. Am. Chem. Soc.* **2015**, *137*, 11507−11516.
(20) Xie, G.; et al. Band inversion induced multiple electronic valleys for high thermoelectric performance of SnTe with strong lattice softening. *Nano Energy* **2020**, *69*, No. 104395.
(21) Pei, Y.; LaLonde, A. D.; Heinz, N. A.; Snyder, G. J. High Thermoelectric Figure of Merit in PbTe Alloys Demonstrated in PbTe-CdTe. *Adv. Energy Mater.* **2012**, *2*, 670−675.
(22) Takagiwa, Y.; Pei, Y.; Pomrehn, G.; Snyder, G. J. Dopants effect on the band structure of PbTe thermoelectric material. *Appl. Phys. Lett.* **2012**, *101*, No. 092102.
(23) Wunderlich, W.; Ohta, H.; Koumoto, K. Enhanced effective mass in doped SrTiO3 and related perovskites. *Phys. B* **2009**, *404*, 2202−2212.
(24) Ohta, S.; Nomura, T.; Ohta, H.; Koumoto, K. High-temperature carrier transport and thermoelectric properties of heavily La- or Nb-doped SrTiO3 single crystals. *J. Appl. Phys.* **2005**, *97*, No. 034106.
(25) Jalan, B.; Stemmer, S. Large Seebeck coefficients and thermoelectric power factor of La-doped SrTiO3 thin films. *Appl. Phys. Lett.* **2010**, *97*, No. 042106.
(26) Okuda, T.; Nakanishi, K.; Miyasaka, S.; Tokura, Y. Large thermoelectric response of metallic perovskites: $Sr_{1-x}La_xTiO_3$. *Phys. Rev. B* **2001**, *63*, No. 113104.
(27) Friedel, J. On Some Electrical and Magnetic Properties of Metallic Solid Solutions. *Can. J. Phys.* **1956**, *34*, 1190−1211.
(28) Pei, Y.; et al. Optimum Carrier Concentration in n-Type PbTe Thermoelectrics. *Adv. Energy Mater.* **2014**, *4*, No. 1400486.
(29) Korringa, J.; Gerritsen, A. N. The cooperative electron phenomenon in dilute alloys. *Physica* **1953**, *19*, 457−507.
(30) Zhu, T.; et al. Hot deformation induced bulk nanostructuring of unidirectionally grown p-type (Bi,Sb) 2 Te 3 thermoelectric materials. *J. Mater. Chem. A* **2013**, *1*, 11589−11594.
(31) Tan, G.; et al. Non-equilibrium processing leads to record high thermoelectric figure of merit in PbTe−SrTe. *Nat. Commun.* **2016**, *7*, No. 12167.
(32) Luo, Z.-Z.; et al. Soft phonon modes from off-center Ge atoms lead to ultralow thermal conductivity and superior thermoelectric performance in n-type PbSe−GeSe. *Energy Environ. Sci.* **2018**, *11*, 3220−3230.
(33) Zhao, L.-D.; et al. Raising the Thermoelectric Performance of p-Type PbS with Endotaxial Nanostructuring and Valence-Band Offset Engineering Using CdS and ZnS. *J. Am. Chem. Soc.* **2012**, *134*, 16327−16336.
(34) Tan, G.; et al. All-Scale Hierarchically Structured p-Type PbSe Alloys with High Thermoelectric Performance Enabled by Improved Band Degeneracy. *J. Am. Chem. Soc.* **2019**, *141*, 4480−4486.
(35) Cai, S.; Luo, Y.; Hu, X.; Kanatzidis, M. G.; Dravid, V. P. All-scale Architecturing of Microstructure in Chalcogenide Thermoelectric Materials. *Microsc. Microanal.* **2019**, *25*, 2236−2237.
(36) Hong, M.; et al. Achieving zT> 2 in p-Type AgSbTe2−xSex Alloys via Exploring the Extra Light Valence Band and Introducing Dense Stacking Faults. *Adv. Energy Mater.* **2018**, *8*, No. 1702333.
(37) Cai, S.; et al. Enhancement of thermoelectric properties by Na doping in Te-free p-type AgSbSe 2. *Dalton Trans.* **2015**, *44*, 1046−1051.
(38) Poudel, B.; et al. High-Thermoelectric Performance of Nanostructured Bismuth Antimony Telluride Bulk Alloys. *Science* **2008**, *320*, 634−638.
(39) Hsu, K. F.; et al. Cubic AgPbmSbTe2+m: Bulk Thermoelectric Materials with High Figure of Merit. *Science* **2004**, *303*, 818−821.
(40) Sales, B. C.; Mandrus, D.; Williams, R. K. Filled Skutterudite Antimonides: A New Class of Thermoelectric Materials. *Science* **1996**, *272*, 1325−1328.
(41) Luo, Y.; et al. High Thermoelectric Performance in Polycrystalline SnSe Via Dual-Doping with Ag/Na and Nanostructuring With $Ag_8SnSe_6$. *Adv. Energy Mater.* **2018**, No. 1803072.
(42) Luo, Z.-Z.; et al. High Figure of Merit in Gallium-Doped Nanostructured n-Type PbTe- *x* GeTe with Midgap States. *J. Am. Chem. Soc.* **2019**, *141*, 16169−16177.
(43) Ding, G.; Si, J.; Yang, S.; Wang, G.; Wu, H. High thermoelectric properties of n-type Cd-doped PbTe prepared by melt spinning. *Scr. Mater.* **2016**, *122*, 1−4.
(44) Qin, D.; et al. Enhanced Thermoelectric and Mechanical Properties in Yb0.3Co4Sb12 with In Situ Formed CoSi Nanoprecipitates. *Adv. Energy Mater.* **2019**, *9*, No. 1902435.
(45) Cai, S.; et al. Discordant nature of Cd in PbSe: off-centering and core−shell nanoscale CdSe precipitates lead to high thermoelectric performance. *Energy Environ. Sci.* **2020**, *13*, 200−211.
(46) Luo, Z.-Z.; et al. Ultralow Thermal Conductivity and High-Temperature Thermoelectric Performance in n-Type $K_{2.5}Bi_{8.5}Se_{14}$. *Chem. Mater.* **2019**, *31*, 5943−5952.
(47) Iordanidis, L.; et al. $A_2Bi_8Se_{13}$ (A = Rb, Cs), $CsBi_{3.67}Se_6$, and $BaBi_2Se_4$: New Ternary Semiconducting Bismuth Selenides. *Chem. Mater.* **2001**, *13*, 622−633.
(48) Zhai, H.; Xiao, Y.; Zhao, L.-D.; Tan, G.; Tang, X. Large effective mass and low lattice thermal conductivity contributing to high thermoelectric performance of Zn-doped Cu5Sn2Se7. *J. Alloys Compd.* **2020**, *826*, No. 154154.
(49) Shi, W.; et al. Tin Selenide (SnSe): Growth, Properties, and Applications. *Adv. Sci.* **2018**, *5*, No. 1700602.
(50) Zhao, L.-D.; et al. Ultrahigh power factor and thermoelectric performance in hole-doped single-crystal SnSe. *Science* **2016**, *351*, 141−144.
(51) Zhao, L.-D.; et al. Ultralow thermal conductivity and high thermoelectric figure of merit in SnSe crystals. *Nature* **2014**, *508*, 373−377.
(52) Chang, C.; et al. 3D charge and 2D phonon transports leading to high out-of-plane ZT in n-type SnSe crystals. *Science* **2018**, *360*, 778−783.
(53) Lee, Y. K.; Luo, Z.; Cho, S. P.; Kanatzidis, M. G.; Chung, I. Surface Oxide Removal for Polycrystalline SnSe Reveals Near-Single-Crystal Thermoelectric Performance. *Joule* **2019**, *3*, 719−731.
(54) Pei, Y.; et al. Multiple Converged Conduction Bands in $K_2Bi_8Se_{13}$: A Promising Thermoelectric Material with Extremely Low Thermal Conductivity. *J. Am. Chem. Soc.* **2016**, *138*, 16364−16371.


https://dx.doi.org/10.1021/acs.chemmater.0c00703
Chem. Mater. XXXX, XXX, XXX−XXX

(55) Kyratsi, T.; Chung, D.-Y.; Ireland, J. R.; Kannewurf, C. R.; Kanatzidis, M. G. Thermoelectric Properties and Site-Selective Rb $^{+}$/K $^{+}$ Distribution in the K $_{2-x}$ Rb $_{x}$ Bi $_{8}$ Se $_{13}$ Series. *Chem. Mater.* **2003**, *15*, 3035−3040.
(56) Zhao, J.; et al. Quaternary Chalcogenide Semiconductors with 2D Structures: Rb $_{2}$ ZnBi $_{2}$ Se $_{5}$ and Cs $_{6}$ Cd $_{2}$ Bi $_{8}$ Te $_{17}$. *Inorg. Chem.* **2018**, *57*, 9403−9411.
(57) Zhao, J.; et al. Homologous Series of 2D Chalcogenides Cs−Ag−Bi−Q (Q = S, Se) with Ion-Exchange Properties. *J. Am. Chem. Soc.* **2017**, *139*, 12601−12609.


https://dx.doi.org/10.1021/acs.chemmater.0c00703
*Chem. Mater.* XXXX, XXX, XXX−XXX